The Role of Moisture Gradients and Time Scales in Wood Mechanosorption

Júlio Amando de Barros[1*] and Falk K. Wittel[1]

[1*]Institute for Building Materials, ETH Zurich, Laura-Hezner-Weg 7, Zurich, 8093, Switzerland ORCID: 0000-0001-6991-2794.

*Corresponding author(s). E-mail(s): jortiz@ethz.ch;
Contributing authors: fwittel@ethz.ch;

Abstract

The mechanical behavior of wood has been widely investigated, but its deformation under combined load and moisture changes remains difficult to describe and predict. The resulting deformation cannot be described by the simple superposition of the individual effects, a phenomenon known as mechanosorption. While mechanosorption is generally attributed to the structural complexity of wood and the rearrangement of hydrogen bonds, key aspects of this phenomenon, including the interplay between viscoelastic and diffusive time scales and the role of internal moisture gradients, remain debated. To address these open questions, a Diffusion-Dependent Stick-Slip Fiber Bundle Model is proposed that couples moisture transport with a mechanical description of deformation mechanisms in hygroresponsive materials. The competition between viscoelastic and diffusion time scales is analyzed through dimensionless numbers across cyclic moisture periods. The results show that longer moisture cycles lead to higher cyclic strain amplitudes, which result in greater mechanosorptive strains. Simulations with and without moisture gradients presented only minor differences in global strain. While gradients induce higher hygromechanical stresses and increased damage, their influence on the overall bundle response is mitigated by the coexistence of tension and compression zones. Finally, surrogate-model-assisted fitting to experimental data showed good agreement with consecutive mechanosorptive and constant-moisture viscoelastic responses. In addition, the results show that mechanosorptive behavior varies significantly across different combinations of mechanical-response parameters, providing insight into the origin of the distinct mechanosorption magnitudes observed in different wood anatomical directions.

Keywords: Mechanosorption, Fiber Bundle Model, Hygro-mechanical, Time Scales

1 Introduction

Wood is a renewable, bio-based material with excellent specific mechanical properties, which has brought it to the center of attention as a key resource for a more sustainable materials industry. Still, the hygroresponsive nature of wood and wood-based materials remains a primary challenge for its long-term usage. In particular, the combination of mechanical load with alternating climatic conditions limits the performance and reliability of such materials in mechanically demanding applications. (Cordeiro 2025; Deshwal et al. 2019; Grottesi et al. 2023; Wang et al. 2020). Over the years, experiments have revealed the main microstructural mechanisms underlying moisture-induced deformation: (i) water molecules infiltrate the hydrogen-bond network between cellulose microfibrils and the surrounding polymer matrix, causing swelling and generating hygric stresses (Salmén 2004, 2015,

2022; Salmén and Burgert 2009; Moliński and Raczkowski 1988; Skaar 1988); (ii) under mechanical load, these moisture-induced changes reduce internal cohesion and facilitate local slippage within this network (Armstrong and Kingston 1960; Eriksson and Norén 1965; Bethe 1969; Raczkowski 1969; Zhang et al. 2021); and (iii) under cyclic moisture conditions, this intermittent stick–slip process accumulates into the mechanosorption effect (Stevanic and Salmén 2020). Depending on loading and moisture conditions, the resulting deformation may stabilize over successive cycles or lead to progressive damage and failure with reduced strength and augmented strain when compared to constant environmental conditions (Hearmon and Paton 1964; Mårtensson 1994).

While there is broad agreement on the general nature and behavior of mechanosorptive effects, authors often diverge on the details. Since the earliest observations, debate has persisted regarding which moisture-related variables primarily govern mechanosorption: some authors attribute it mainly to moisture fluxes and their rates (Bažant 1985; Mårtensson 1988), whereas others emphasize only the amplitude of the moisture cycle itself (Gibson 1965; Armstrong and Grossman 1972; Gunderson and Tobey 1990). The importance of characteristic time scales further complicates this discussion, for example, it was found for Kevlar fibers that mechanosorptive effects only appear under specific cyclic periods (Habeger et al. 2001). Beyond time-scale effects, inconsistencies in the literature are amplified by the intermixing of different loading modes, material orientations, and length scales. For example, the largest mechanosorptive strain increment consistently occurs during the first moisture cycle, whereas an additional increase during the first drying phase is observed in bending but not in uniaxial loading (Armstrong and Christensen 1961; Hunt and Shelton 1987; Dubois et al. 2012; Ferrara and Wittel 2025b). Differences in the relative contributions of elastic, viscoelastic, plastic, and hygroexpansive mechanisms, governed by the material structure across orientations and scales, strongly affect the evolution and magnitude of mechanosorptive behavior (Olsson et al. 2007; Dong et al. 2010; Amando de Barros et al. 2025; Maas and Wittel 2026). Although these behaviors arise from a common underlying moisture–material interaction mechanism, their manifestation depends strongly on the specific combination of governing material and loading parameters. This motivates the need for a theoretical framework that captures the fundamental process while enabling systematic exploration of its consequences across different conditions.

Statistical models provide a framework in which local constitutive rules and interactions are defined at the fiber level, allowing macroscopic behavior to emerge from collective dynamics (Alava et al. 2006; Herrmann and Roux 1990; Phoenix and Beyerlein 2000). Among these, the Fiber Bundle Model (FBM) is particularly suited for fibrous materials and has been successfully applied to describe damage evolution in wood (Dill-Lager et al. 2003; Hidalgo et al. 2002). Specifically for mechanosorption, a moisture-dependent stick-slip FBM was developed that integrates hygro-mechanical mechanisms with material heterogeneity (Amando et al. 2024). In the current work, this model is modified to be coupled with moisture-transport simulations to investigate how moisture gradients, and diffusion and viscoelastic time scales affect mechanosorptive strain. By systematically varying these parameters, their relative contributions and combined effects can be assessed.

The manuscript is organized as follows: Materials and Methods (Sec. 2) outlines the mathematical model formulation, the coupling to moisture transport, and the

analytical procedures used to quantify viscoelastic and mechanosorptive behavior. Results and Discussion (Sec. 3) reports the model sensitivity to moisture-cycling times, and the influence of moisture gradients, as well as the comparison to recent experimental data. The Conclusions (Sec. 4) summarizes the main findings and connects them to the broader questions in the field.

2 Materials and Methods

The modeling framework to implement the coupled Diffusion–Dependent Stick–Slip Fiber Bundle Model (DD-SS-FBM), as well as the main analysis approach used in this study, are presented in the following sequence: the mechanical model formulation (Sec. 2.1), the moisture transport simulations (Sec. 2.2), an approach to unify time scales between moisture cyclic time and diffusion and viscoelastic characteristic times (Sec. 2.3), a macroscopic strain decomposition approach to facilitate experimental comparison (Sec. 2.4), and the parameters and simulations set investigated (Sec. 2.5).

2.1 Mathematical Model Formulation

The simplest form of a Fiber Bundle Model (FBM) (Daniels 1945) consists of an assembly of N Hookean fibers that share identical compliances but differ in strength, typically represented by fiber-specific failure strain thresholds ε_i^{th} sampled from a Weibull distribution (Weibull 1951). When a load F is applied, each fiber i carries an equal share, $F_i = F/N$, and deforms with a strain ε_i. Once a fiber reaches its failure threshold ε_i^{th}, it fails and its load is redistributed among the remaining fibers. This process introduces a non-linear relation between F and the macroscopic bundle strain ε, governed by the threshold distribution. Different material responses can be incorporated by modifying the load sharing rules (local or global) or the constitutive behavior of the fibers, for instance by replacing elastic fibers with Kelvin-Voigt (KV) bodies to capture viscoelasticity (Hidalgo et al. 2002; Kun et al. 2000; Zhang and Ding 1996). Halász and Kun (2009) proposed a stick-slip extension in which fibers do not fail upon reaching their threshold, but instead release their load and store the corresponding strain threshold as a slip deformation, and remain attached to the bundle to be further loaded. This allows repeated slip events and accumulation of slip strain. Still, after a predefined number of slip events, the fiber could break, and the bundle would be permanently damaged. As discussed in the introduction, such stick-slip behavior is consistent with bond detachment and reformation mechanisms in fibrous materials like wood (Stevanic and Salmén 2020; Zhang et al. 2021). Consequently, the stick-slip FBM was adopted as the starting point for a mechanosorptive model.

In wood, deformation processes are further influenced by changes in moisture content, which alter mechanical properties and affect the stick-slip mechanism. To address this, a Moisture-Dependent SS-FBM (MD-SS-FBM) was proposed (Amando et al. 2024). Each fiber of the MD-SS-FBM comprises a series of four rheological components: an elastic spring, a viscoelastic KV body, a hygroexpansive component, and a slip component accounting for cumulated slip strains. Additional rules were introduced to extend the SS-FBM to couple hygro-mechanical conditions and reproduce the effects of varying moisture. Three main assumptions were implemented:

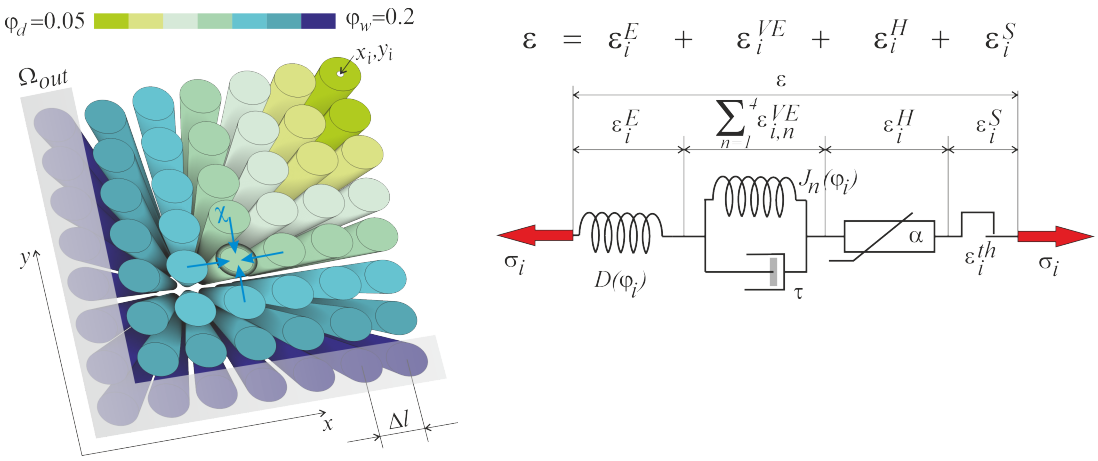

Fig. 1: Schematic of the coupled hygro-mechanical model. The represented mechanical parameters are: D, elastic compliance; J_n, viscoelastic compliance for a Generalized Kevin-Voigt element; τ, viscoelastic characteristic time; α, hygroexpansion coefficient; and ε_i^{th}, the slip threshold value. The moisture parameters represented are: φ_i, the local moisture content; φ_d and φ_w, the dry and wet moisture contents; χ, the diffusion coefficient; and Ω_{out}, the set of outer fibers where the moisture boundary conditions are applied.

1. *Moisture-dependent compliances:* elastic and viscoelastic compliances increase with moisture;
2. *Bidirectional slip:* backward slip is allowed if a fiber is compressed, for example during drying shrinkage, allowing recovery of slip strains;
3. *History-, moisture-, and direction-dependent thresholds:* the slip thresholds decrease progressively with accumulated slip events, increasing moisture, or reverse slip direction.

In this work, moisture transport is applied to the MD-SS-FBM, generating the DD-SS-FBM, schematically shown in Fig. 1, which requires modifications to the original mathematical formulation (Amando et al. 2024). A schematic visualization of the DD-SS-FBM is presented in Fig. 1.

The strain at time t of a fiber i that has slipped k_i times, has local moisture content φ_i, and is subjected to a local stress $\sigma_i = F_i/A_i$, where $A_i = 1 \forall i$, is given by

$$\begin{aligned}\varepsilon_i(\sigma_i, \varphi_i, t) &= \varepsilon_i^E(\sigma_i, \varphi_i) + \varepsilon_i^{VE}(\sigma_i, \varphi_i, t) + \varepsilon_i^H(\varphi_i) + \varepsilon_i^S(k_i, \varphi_i, \beta_i) \\ &= D(\varphi_i)\,\sigma_i + \sum_{n=1}^{4} J_n(\varphi_i)\,\sigma_i\left(1 - e^{-t/\tau_n}\right) \\ &\quad + \alpha\left(\varphi_i - \varphi_0\right) + \sum_{j=1}^{k_i(t)} \varepsilon_i^{th}(j).\end{aligned} \tag{1}$$

The four contributions correspond to the *elastic*, *viscoelastic*, *hygroexpansive*, and *slip* components, respectively. Here, $D(\varphi_i)$ is the moisture-dependent elastic compliance; $J_n(\varphi_i)$ are the moisture-dependent viscoelastic compliances of a Generalized-KV element with four elements ($n = [0, 1, 2, 3]$), each with a characteristic relaxation time $\tau_n = 10^n \tau_0$; α is the hygroexpansion coefficient; φ_0 is the initial moisture content; $k_i(t)$ is the number of slip events experienced by the fiber i up to time t; and $\varepsilon_i^{th}(j)$ is the slip threshold at the j-th slip event, which depends on the fiber's moisture, direction (represented here as β_i), and slip history.

In the model, a global load sharing scheme is used, therefore $\varepsilon_i = \varepsilon \forall i$, and to compute ε the stress per fiber, σ_i, must be written as

$$\sigma_i = \varepsilon_i^E / D_i = \left(\varepsilon - \varepsilon_i^{VE} - \varepsilon_i^H - \varepsilon_i^S\right)/D_i. \tag{2}$$

By imposing $F = \sum_{i=1}^{N} \sigma_i$, the total strain is written as

$$\varepsilon = \left[F + \sum_{i=1}^{N} \left((\varepsilon_i^{VE} + \varepsilon_i^H + \varepsilon_i^S)/D_i\right)\right] \cdot \left(\sum_{i=1}^{N} \left(1/D_i\right)\right)^{-1}. \tag{3}$$

The slip condition of each fiber is given by

$$\varepsilon_i^E + \varepsilon_i^{VE} > f(k)\Gamma_\varphi \Gamma_\beta \varepsilon_i^{th}, \tag{4}$$

where $f(k)$ is the history-dependent weakening function of the slipping threshold, Γ_φ is the moisture-dependent rescaling factor, and Γ_β is the directional-dependent rescaling factor.

With the presented formulation, it is now possible to calculate the bundle's strain for a non-homogeneous moisture field. To compute realistic moisture distributions within the system, moisture-transport simulations were performed as described below.

2.2 Moisture Transport Simulations

Below the fiber saturation point, water in wood exists as bound water and vapor (Skaar 1988). While multi-Fickian models are often used to distinguish these contributions (Frandsen et al. 2007), a single Fickian diffusion process with moisture-dependent diffusivity values is adopted here for simplicity. The diffusivity is chosen to represent empirical ranges across the moisture content interval from dry ($\varphi_d = 0.05$) to wet ($\varphi_w = 0.20$) states, where variations of approximately one order of magnitude are observed in radial and tangential directions (Sonderegger et al. 2011; Niemz et al. 2023). Accordingly, the implemented moisture transport dynamics follow

$$\frac{\partial \varphi_i}{\partial t} = \nabla \cdot \left(\chi_i(\varphi_i) \nabla \varphi_i\right), \tag{5}$$

$$\chi_i(\varphi_i) = \chi_d \exp\left[\frac{\ln 10}{\varphi_w - \varphi_d}\left(\varphi_i - \varphi_d\right)\right], \tag{6}$$

where χ_i is the moisture-dependent diffusion coefficient, and χ_d, set to 1 for simplicity, is the reference diffusivity at φ_d, the numerical implementation is detailed in Appendix A.1.

Moisture transport was computed by initializing all fibers at φ_d and prescribing the environmental moisture history $\varphi_{\text{env}}(t)$ as a boundary condition on the outermost fibers, Ω_{out},

$$\varphi_i = \varphi_{\text{env}}(t), \qquad i \in \Omega_{\text{out}}. \tag{7}$$

The environmental moisture change was prescribed as a transition from $\varphi_{\mathrm{i}} \to \varphi_{\mathrm{f}}$ starting at t_0, with ramping time T_r:

$$\varphi_{\mathrm{env}}(t) = \begin{cases} \varphi_{\mathrm{i}}, & t < t_0, \\ \varphi_{\mathrm{i}} + \dfrac{t - t_0}{T_r}\big(\varphi_{\mathrm{f}} - \varphi_{\mathrm{i}}\big), & t_0 \le t < t_0 + T_r, \quad T_r > 0, \\ \varphi_{\mathrm{f}}, & t \ge t_0 + T_r, \end{cases} \tag{8}$$

with the limiting case $T_r = 0$ corresponding to an instantaneous step transition. Here, $\varphi_{\mathrm{i}} \to \varphi_{\mathrm{f}}$ denotes either a wetting ($\varphi_{\mathrm{d}} \to \varphi_{\mathrm{w}}$) or drying ($\varphi_{\mathrm{w}} \to \varphi_{\mathrm{d}}$) transition.

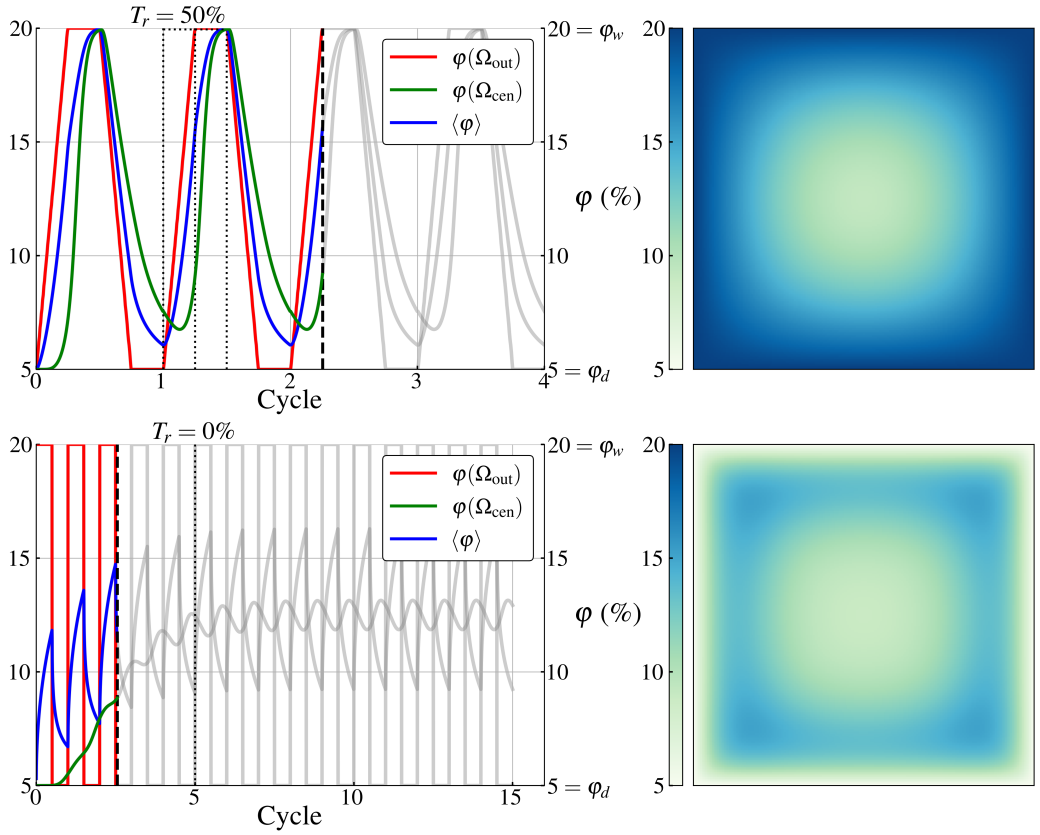

Fig. 2: Moisture content profile for simulations with quick diffusion with ramping time $T_r = 50\%$ (top), and slow diffusion with $T_r = 0\%$ (bottom). $\varphi(\Omega_{\mathrm{out}})$ is the moisture content of the most outer fibers and represented by the red curves (boundary condition); $\varphi(\Omega_{\mathrm{cen}})$ the moisture content of the central fibers and represented in green; $\langle\varphi\rangle$ the bundle average represented in blue. The dashed black line marks the snapshot time for the heatmaps, and the dotted lines mark the moisture ramping $T_r = 50\%$ (top) and $T_r = 0\%$ (bottom).

Moisture evolution was simulated under cyclic dry–wet–dry boundary conditions, alternating between φ_d and φ_w with a fixed period T_c and ramping time T_r. Simulations were repeated until a steady cyclic regime was reached, defined by a relative change in the average bundle moisture $\langle\varphi_i\rangle$ below $10^{-8}\%$ between consecutive cycles. For mechanical simulations requiring additional cycles, the final steady moisture cycle was repeated. Examples of the resulting moisture profiles are shown in Fig. 2. Due to the moisture-dependent diffusion coefficient, moistening proceeds faster than drying, leading to asymmetric evolution. For short cycle periods T_c, strongly inhomogeneous moisture profiles develop, with central fibers Ω_{cen}

not reaching the moisture extremes φ_d and φ_w, whereas longer cycles allow more homogeneous moisture distributions. Additionally, uniform moisture profiles were assigned by prescribing the spatial average $\langle\varphi_i\rangle$ to all fibers (blue lines in Fig. 2), enabling isolation of moisture-gradient effects (see Sec. 3.3).

It is important to note that this formulation is scale-invariant: the moisture evolution depends only on the relative magnitudes of the diffusion coefficient, bundle size, and cycle period. Consequently, the governing parameter is the ratio between the characteristic diffusion time and the imposed cycle time, which determines the degree of equilibration within each cycle. This motivates the introduction of dimensionless numbers to analyze the model behavior, as explained in the following section.

2.3 Unifying Time Scales

A central challenge in the usage of hygroresponsive viscoelastic materials is the multiple competing time scales, namely, 1) the moisture diffusion, 2) the viscoelastic relaxation (bundle-internal properties), and 3) the environmental moisture cycle period T_c. Comparing their relative influence across different materials and conditions, therefore, requires a common framework. To achieve this, we express each process in relation to the cycle time. This leads naturally to the definition of Fourier-type numbers,

$$Fo_\chi = \frac{T_c}{T_\chi}, \qquad Fo_\tau = \frac{T_c}{T_\tau}, \tag{9}$$

where T_χ and T_τ are characteristic times for diffusion and viscoelastic relaxation, respectively. These quantities measure how much each internal process can evolve within each change in environmental conditions: a large Fo corresponds to near-complete relaxation within each change (half of a cycle), while a small Fo indicates strongly out-of-equilibrium situations.

The choice of T_χ and T_τ is not universal, but should capture the dominant kinetics of each process. Both moisture diffusion and viscoelastic relaxation exhibit a similar temporal evolution, characterized by a rapid initial response followed by a slow approach to equilibrium. Accordingly, the characteristic times T_χ^Y and T_τ^Y are here defined as the time required to reach $Y\%$ of the final state: the average bundle moisture $\langle\varphi_i\rangle$ reaching $Y\%$ of φ_{env}, and the time-dependent creep compliance $J(t) = J\big(1 - \mathrm{e}^{-t/\tau}\big)$ reaching $Y\%$ of its asymptotic value J (Fig. 3). The corresponding Fourier numbers are

$$Fo_\chi^Y = \frac{T_c}{T_\chi^Y}, \qquad \text{where } \langle\varphi\rangle\big(T_\chi^Y\big) = \frac{Y}{100}\,\varphi_{env}, \tag{10}$$

$$Fo_\tau^Y = \frac{T_c}{T_\tau^Y}, \qquad \text{where } J\big(T_\tau^Y\big) = \frac{Y}{100}\,J. \tag{11}$$

In this work, $Y = 99$ is selected since it represents near-complete equilibration. For example, $Fo^{99} = 2$ indicates that each half-cycle is sufficient for the system to reach approximately 99 % of its diffusive or viscoelastic relaxation before changing φ_{env}. The influence of this choice is further examined in Sec. 3.

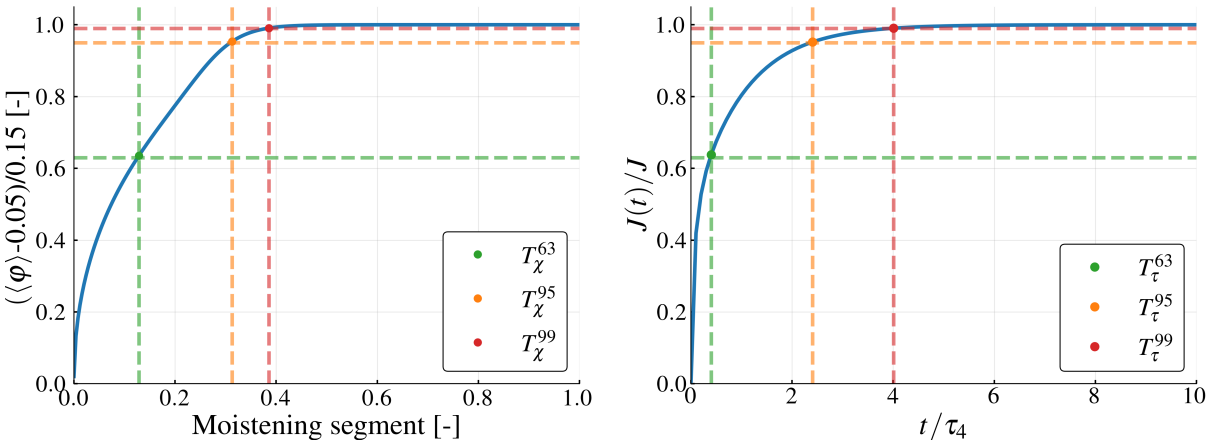

(a) (b)

Fig. 3: Examples of different criteria ($Y = [63, 65, 99]$ in Eq. 10 and Eq. 11) to define characteristic times for moisture transport (a) and viscoelasticity (b).

To merge the effects of both internal processes into a single metric, an effective Fourier number is defined as

$$Fo_{\text{eff}}^{Y} = \left(Fo_{\chi}^{Y}\right)^{a}\left(Fo_{\tau}^{Y}\right)^{b} e^{(cT_r)}, \tag{12}$$

where the exponents a and b represent the relative influence of diffusion and viscoelasticity, respectively. The last term accounts for the effect of the ramping time T_r and takes an exponential form to act as a damper on the diffusion process; its influence is weighted by the parameter c. The procedure used to determine these coefficients is discussed in Sec. 3.2.

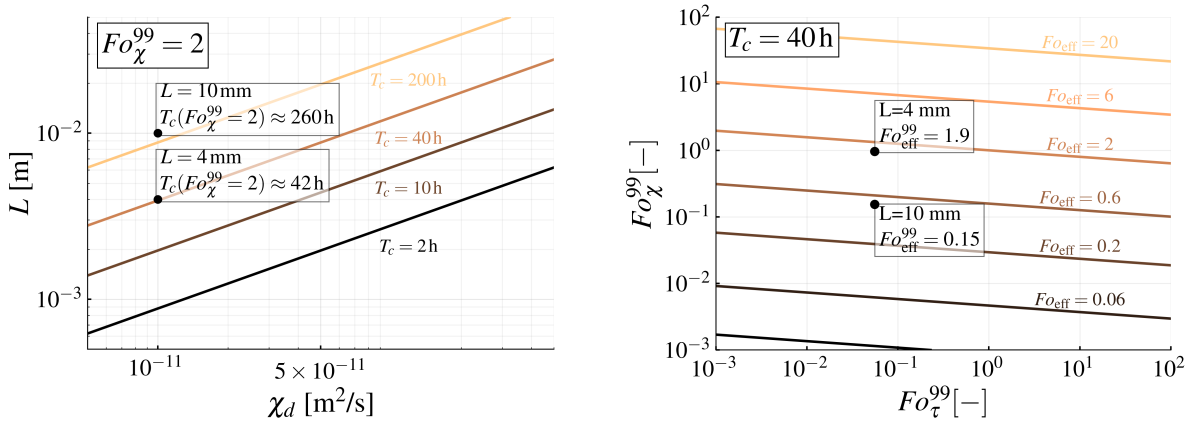

(a) (b)

Fig. 4: Fourier-number tuning in parameter space. (a) Parameter combinations for a squared sample with size L and dry-state diffusion coefficient χ_d yielding iso-lines of cyclic time for $Fo_\chi^{99} = 2$ and $T_r = 0\%$. (b) Parameter combinations of Fo_τ^{99} and Fo_χ^{99} defining iso-lines of Fo_{eff}, using the parameters obtained in Sec. 3, for a fixed cyclic time of 40 h.

Defining dimensionless numbers in this way enables direct experimental application. The characteristic times T_χ^Y and T_τ^Y can be obtained from transient moisture measurements and standard viscoelastic tests, respectively, while the Fourier numbers Fo_X^Y can be tuned by adjusting the cycle period T_c. Figure 4 illustrates the

tunning of Fo_{χ}^{99} and Fo_{τ}^{99} using experimental values of χ_d (Niemz et al. 2023), squared samples with size $L = 4$ and 10 mm, and viscoelastic parameters reported for radial direction by Ferrara and Wittel (2025a). In summary, maintaining a constant Fo_{χ}^{99} for increasing sample sizes L or decreasing diffusion coefficients χ_d requires increasing T_c to compensate for slower equilibration. Conversely, for a fixed T_c, different combinations of Fo_{χ}^{99} and Fo_{τ}^{99} lead to distinct effective responses, as summarized by Fo_{eff} (Fig. 4b) using the parameters obtained in Sec. 3. Finally, to enable comparison with experiments, a protocol is introduced to relate the simulated bundle strain to measurable macroscopic strains, as described in the following section.

2.4 Macroscopic Strain Decomposition for Experimental Comparison

In the DD-SS-FBM, the strain of each bundle fiber and its individual contributions—elastic, viscoelastic, hygroexpansive, and slip—are directly accessible. At the macroscopic level, the total strain can therefore be expressed as the sum of these components (see Eq. 3). In experiments, however, only the total strain $\varepsilon(t)$ is measurable, and any decomposition into individual contributions must be inferred through post-processing. To enable a consistent comparison between simulations and experiments, a translation framework is therefore required.

The strain decomposition used in this work follows the protocol proposed by Ferrara and Wittel (2025b), in which the measured strain is decomposed as

$$\varepsilon(t) = \varepsilon^{*E}(t) + \varepsilon^{*VE}(t) + \varepsilon^{*H}(t) + \varepsilon^{*MS}(t), \tag{13}$$

being the elastic, viscoelastic, hygroexpansive, and mechanosorptive contributions, respectively, and $*$ denotes quantities obtained by post-processing of the measured strain. The decomposition proposed in Ferrara and Wittel (2025b) proceeds as follows:

1. *Viscoelastic strain calculation:* The moisture-dependent experimental viscoelastic compliance, $J_{exp}(\varphi)$, is obtained from creep experiments performed at multiple constant moisture levels (e.g., $\varphi = 0.05, \ldots, 0.2$) using a generalized Kelvin–Voigt model to fit the results. The obtained compliance was then used to compute ε^{*VE} based on the load and moisture history during the mechanosorptive experiment.
2. *Reduced strain calculation:* a reduced strain is defined as $\varepsilon^{*R}(t) = \varepsilon(t) - \varepsilon^{*VE}(t)$, which contains elastic, hygroexpansive, and mechanosorptive contributions by definition.
3. *Hygroelastic strain calculation:* Assuming a decreasing mechanosorptive contribution over cycles, the last loaded cycle is considered as the one with the lowest mechanosorptive influence. The ε^{*R} in this cycle is therefore used as a reference strain template for the combined hygroexpansion and elastic response. To eliminate any remaining mechanosorptive effects, the template is corrected by removing residual drift such that its initial and final strains coincide. A linear relationship between the corrected strain template and the average moisture content $\langle \varphi_i \rangle$ is then assumed within this cycle, and a corresponding linear coefficient is obtained. This coefficient is subsequently used to reconstruct the

hygroelastic strain in all other cycles by scaling the reference template according to the cycle-specific moisture variation, i.e., based on the difference between initial and final moisture levels in each cycle. In this way, the hygroelastic contribution $\varepsilon^{*HE} = \varepsilon^{*H} + \varepsilon^{*E}$ is determined for all loaded cycles. The same procedure is then applied to the unloaded cycles. See Fig. 6 for a visual representation.

4. *Mechanosorptive strain calculation:* $\varepsilon^{*MS}(t)$ is finally defined as $\varepsilon^{*R}(t) - \varepsilon^{*HE}(t)$.

To reproduce this procedure within the DD-SS-FBM, a series of simulations was performed under constant load, each at a different fixed moisture level, thereby mimicking creep tests at constant moisture. This step is needed for defining an effective bundle compliance $J_{eff}(\varphi)$, which differs from the fiber creep compliance $J(\varphi)$ due to the slip strains accumulated in the test. This approximates $J_{eff}(\varphi)$ to the experimental viscoelastic compliance, $J_{exp}(\varphi)$, explained in item 1 above.

Two extensions are possible to be introduced with the model to enrich the analysis: (i) the inclusion of *plastic strain* ε^{*P}, and (ii) the decomposition of mechanosorption into *recoverable* and *non-recoverable strain* components, $\varepsilon^{*MS} = \varepsilon^{*MSr} + \varepsilon^{*MSnr}$. The plastic strain ε^{*P} is identified from scleronomous simulations at fixed moisture. The model is loaded and unloaded, and the residual strains are defined as ε^{*P}. This procedure is repeated over a range of load levels and moisture states, allowing ε^{*P} to be expressed as a function of the maximum load and maximum average moisture experienced by the bundle. The non-recoverable mechanosorptive strain, $\varepsilon^{*MSnr}(C_L)$, is defined as the residual strain remaining after C_L loaded moisture cycles. After these cycles, the load is removed, and additional moisture cycles are applied until a steady cyclic response is reached. The remaining strain after this procedure is taken as $\varepsilon^{*MSnr}(C_L)$.

Through this procedure, all strain components of the DD-SS-FBM are mapped onto experimentally accessible quantities, enabling direct comparison between simulated and measured responses under cyclic hygro-mechanical loading.

2.5 Summary of Parameters and Simulations

The DD-SS-FBM mechanical and slip threshold parameters were adopted from the original formulation, where the proportionality between parameters refers to the typical ranges measured for the longitudinal direction of wood, and are summarized in Tab. 1 (Amando et al. 2024; Maas and Wittel 2026). As the parameters are defined in a dimensionless manner, loads and strains are normalized by the critical load, σ_c, and critical strain, ε_c, of the DD-SS-FBM in the wet state. Further details on the numerical implementation used to ensure numerical accuracy and reduce computational cost are provided in Appendix A.2.

The simulation campaign is organized into four groups, each addressing a specific aspect of the model analysis (Tab. 1).

(i) Macroscopic strain decomposition simulations: scleronomic load-unload tests are used to identify plastic strains ε^{*P}, while creep simulations at constant moisture determine the effective viscoelastic compliance $J_{eff}(\varphi)$, and ε^{*MSnr} is calculated via a series of simulations, each with increasing number of loaded moisture cycles, followed by unloading and sufficient unloaded moisture cycles to reach steady cycles.

Table 1: Model parameters and ranges used in the simulations.

Parameter	Value / Range	Description
Bundle and simulation properties		
N	40000	Number of fibers
σ_c	1.8	Critical load at wet state
Fiber mechanical properties		
D_d	1	Dry elastic compliance
D_w	1.3	Wet elastic compliance
J_d	0.2	Dry creep compliance
J_w	0.4	Wet creep compliance
α	0.5	Hygroexpansion coefficient
τ_n	$[1, 10, 100, 1000]$	Creep characteristic times
Threshold and stick–slip parameters		
m	2	Weibull shape parameter
λ	7	Weibull scale parameter
d	11	Degradation parameter
κ^f	0.3	Failure limit
Γ_m	0.7	Moisture scaling factor
Γ_β	0.75	Direction scaling factor
Parameters range for analysis:		
(i) Macroscopic strain decomposition simulations - Sec. 3.1		
σ/σ_c	$[0.05, 0.7]$	Load degree
φ	[0.05, 0.2]	Constant moisture for creep simulations
σ/σ_c	0.7	Load degree for Fig. 6
Fo_χ^{99}	2.15	Diffusion Fourier number for Fig. 6
Fo_τ^{99}	0.7	Viscoelastic Fourier number for Fig. 6
(ii) Time-scale simulations - Sec. 3.2		
σ/σ_c	0.7	Load degree
σ/σ_c	[0.2, 0.7]	Load degrees for Fig. 9
Fo_χ^{99}	[3.22, 2.15, 1.07, 0.32, 0.11]	Diffusion Fourier numbers
Fo_τ^{99}	$50.30 \times [1, 0.1, 0.01, 0.001]$	Viscoelastic Fourier numbers
T_r	{0, 0.1, 0.3, 0.5}	
(iii) Uniform moisture profile simulations - Sec. 3.3		
Same range as Sec. 3.2, but with uniform moisture profile		
(iv) Experimental comparison simulations - Sec. 3.4		
Parameters discussed in Sec. 3.4		

(ii) Time-scale simulations: the model is evaluated over a wide parameter space defined by diffusion and viscoelastic Fourier numbers, Fo_χ^{99} and Fo_τ^{99}, as well as ramping fractions T_r, enabling systematic exploration of regimes ranging from near-equilibrium to strongly non-equilibrium moisture cycling.

(iii) Uniform moisture profile simulations: the same parameter space as *(ii)* is analyzed under uniform moisture profiles based on the bundle-average moisture, excluding the influence of spatial gradients.

(iv) Experimental comparison simulations: additional simulations are performed to reproduce experimental observations, with the corresponding parameter selection discussed in Sec. 3.4.

3 Results and Discussion

The main results obtained from the simulation campaign, summarized in Tab. 1, are described in this section. It covers the strain decomposition and its consistency with experimentally observed behavior (Sec. 3.1), the influence of time-scale competition on mechanosorptive strain accumulation (Sec. 3.2), the role of moisture gradients through comparison of heterogeneous and uniform moisture profiles (Sec. 3.3), and a case study comparing model behavior with experimental data (Sec. 3.4).

3.1 Strain Decomposition

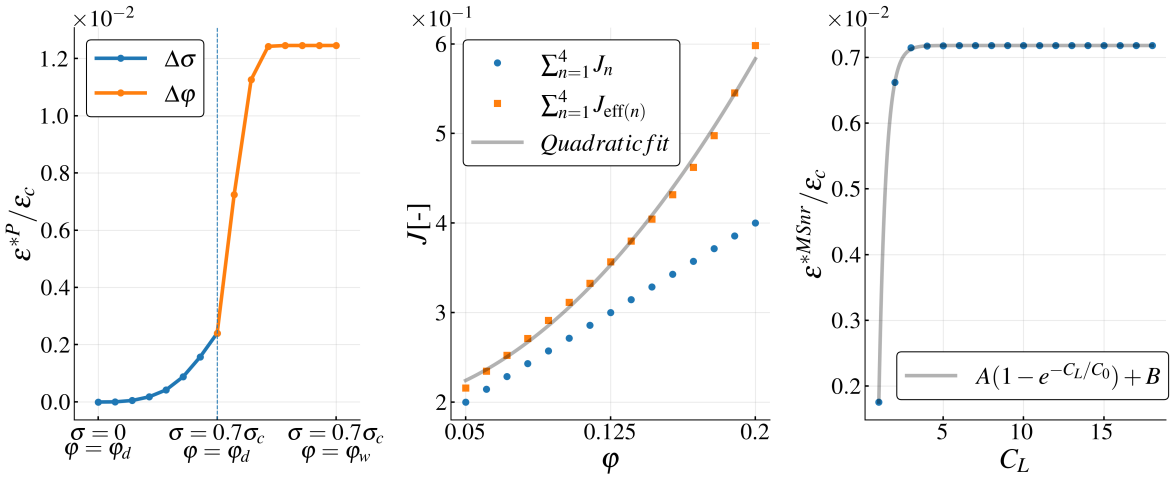

Fig. 5: a) Plastic strain obtained via scleronomic tests with increasing load level (first half), and increasing moisture content (second half). b) Quadratic fit of effective viscoelastic compliance, J_{eff}, for varying moisture content, φ. c) Example of exponential fit of non-recoverable mechanosorptive strain for varying number of moisture cycles

To evaluate the physical consistency of the strain decomposition, the evolution of the individual deformation mechanisms in relation to moisture content and loading degree is analyzed. A strong moisture sensitivity of irreversible deformation is observed: the plastic strain ε^{*P} increases by up to a factor of six from dry to wet conditions (Fig. 5a), in agreement with recent experimental observations (Maas and Wittel 2026).

The viscoelastic bundle response exhibits a pronounced nonlinear (quadratic-like) dependence on moisture, even though a linear dependence is imposed at the fiber level (Fig. 5b), indicating that nonlinear bundle behavior emerges even when the local response is considered linear. This resulting quadratic trend and the effective compliance values are consistent with reported viscoelastic behavior and variation range of wood tissues in longitudinal direction (Ferrara and Wittel 2025a).

The full strain decomposition is shown in Fig. 6 and illustrates the relation between the macroscopic strain and its individual components. Two approaches are compared: (i) the decomposition obtained directly from the internal variables of the DD-SS-FBM (top plot), and (ii) a decomposition derived from the macroscopic strain following the procedure described in Sec. 2.4 (middle plot). It is evident that slip (light gray line in the top plot), obtained directly from the model, and

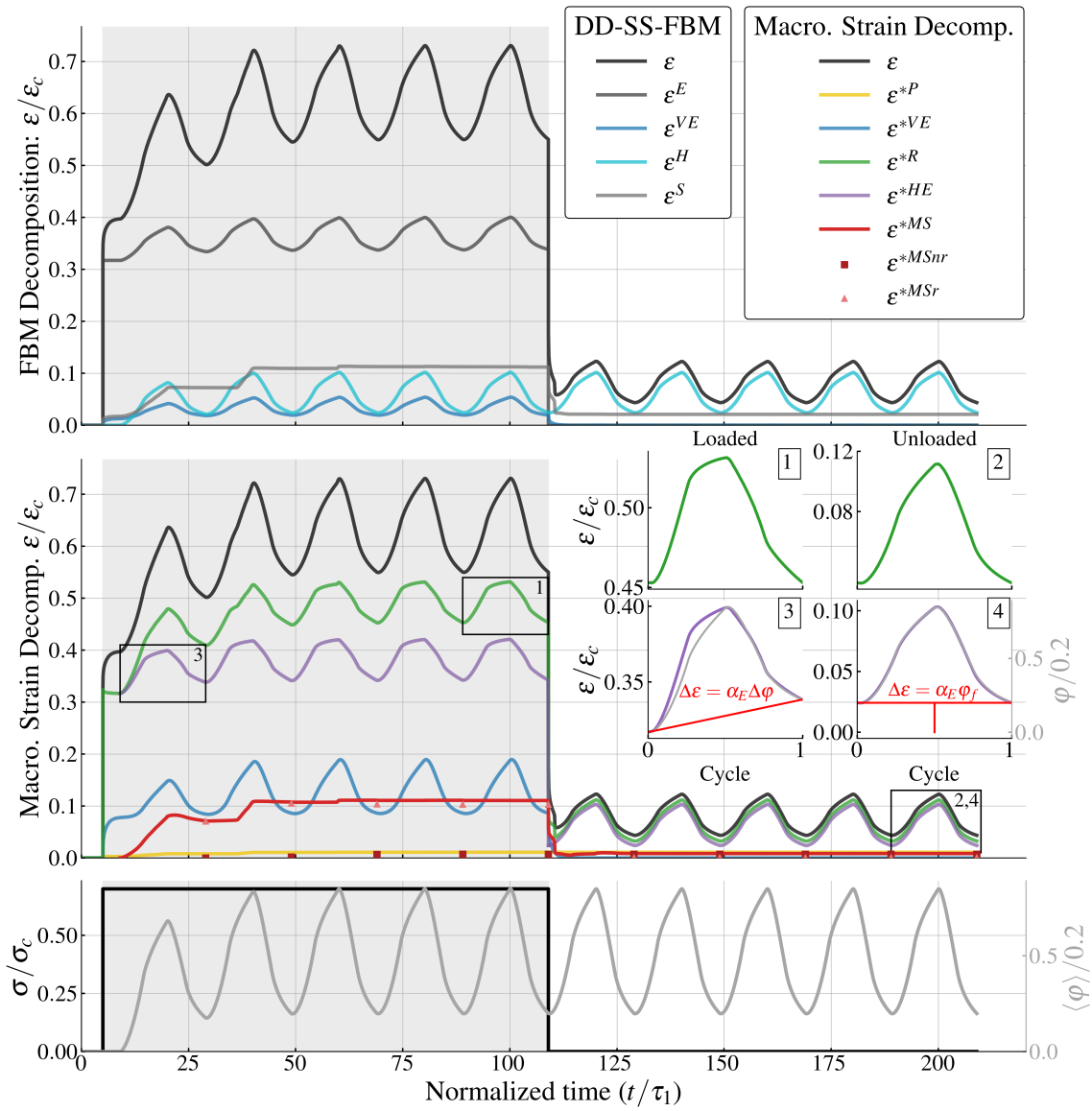

Fig. 6: Macroscopic strain decomposition for a system with $Fo_\chi^{99} = 2.15$, $Fo_\chi^{99} = 0.7$, $T_r = 30\%$ and $\sigma/\sigma_c = 0.7$. ε is the total simulated strain; ε^{*P} is the calculated scleronomic plastic strain; ε^{*VE} is the calculated viscoelastic strain from the fitted effective compliances; $\varepsilon^{*R} = \varepsilon - \varepsilon^{*P} - \varepsilon^{*VE}$ is the reduced strain; ε^{*HE} is the hygroelastic strains built from the reduced strain (see inset plots for the loaded cycles, left, and unloaded, right); and ε^{*MS} is the calculated mechanosorptive strain with its recoverable, ε^{*MSr}, and irrecoverable,ε^{*MSnr}, components calculated per cycle C_L.

mechanosorptive strain (red line in the middle plot), obtained from the macroscopic decomposition, exhibit similar behavior and comparable magnitudes. This agreement is noteworthy because the two quantities rely on different definitions of viscoelastic compliance, namely the bundle effective compliance, J_{eff}, and the fiber-level compliance, J. This apparent consistency arises from a compensation between viscoelastic and hygroelastic contributions. While ε^{*VE} is overestimated relative to ε^{VE}, the hygroelastic contribution ε^{*HE} (green line in the middle plot) is underestimated relative to $\varepsilon^E + \varepsilon^H$ (dark gray and light blue lines in the top plot). As a result, much of the discrepancy between the two decompositions is balanced. Consequently, the remaining difference between ε^S and ε^{*MS} is primarily associated with the plastic strain, ε^{*P}, which is an order of magnitude smaller.

This supports the interpretation of mechanosorption as a collective manifestation of stick–slip processes at the bundle scale. Moreover, the mechanosorptive increment rapidly decreases and stabilizes after two to three cycles, as discussed in more detail in Sec. 3.4, where additional parameter combinations are explored. Although a large fraction of the mechanosorptive strain develops in the first cycle, it is predominantly recoverable, whereas the non-recoverable component, ε^{*MSnr}, builds up mainly during the second cycle (see Fig. 5c) for the system.

3.2 Time Scale Effects in Mechanosorption

To assess the influence of time scales on mechanosorption, the mechanosorptive strain is evaluated across all combinations of diffusion (Fo_χ^{99}), viscoelastic (Fo_τ^{99}), and ramping (T_r) parameters. As these combinations lead to varying contributions from the other strain components (elastic, hygroexpansive, and viscoelastic), the mechanosorptive strain is normalized by the total strain, $\varepsilon^{*MS}/\varepsilon$, yielding the fraction of deformation attributable to mechanosorption. Furthermore, the evolution of mechanosorptive strain across cycles depends strongly on the governing time scales, leading to distinct transient behaviors. To enable consistent comparison, a steady mechanosorptive strain, ε_∞^{MS}, is defined as the value of ε^{*MS} once no further slip develops between consecutive cycles. This condition is used as the criterion to trigger unloading in the model. The results analyzed here are therefore expressed in terms of $\varepsilon_\infty^{*MS}/\varepsilon_\infty$.

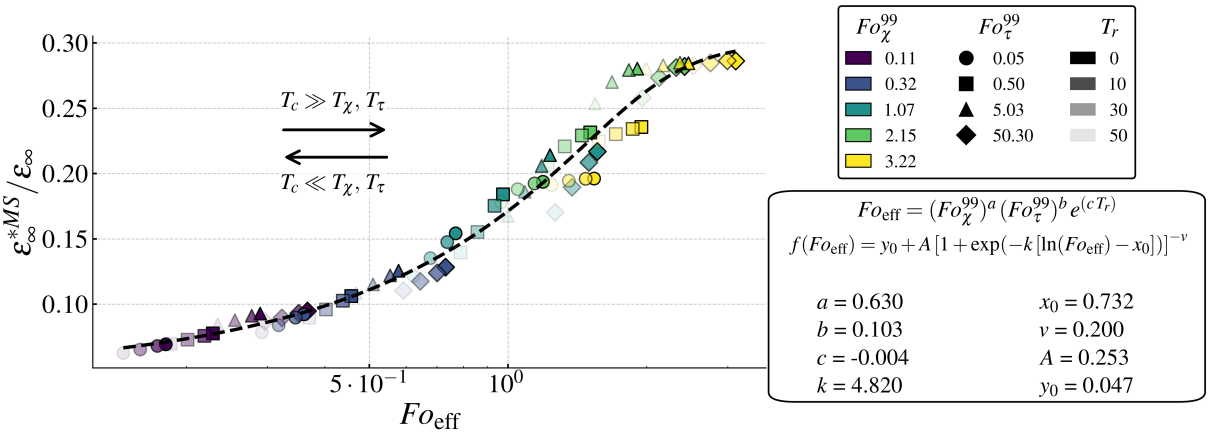

Fig. 7: Mechanosorptive contribution on total strain as a function of Fo_{eff}.

The dependence of $\varepsilon_\infty^{*MS}/\varepsilon_\infty$ on the governing time scales is quantified through a joint mean-square-error minimization, in which both the parameters of a logistic function and the coefficients defining the effective Fourier number Fo_{eff} are determined simultaneously. This results in a collapse of all simulation data onto a single master curve (Fig. 7), indicating that the proposed formulation captures the dominant time-scale dependencies of the system. The master curve shows that mechanosorptive strain increases by up to $5\times$ as Fo_{eff} increases, i.e., from short cycles ($Fo_{eff} \lesssim 0.5$) to long cycles ($Fo_{eff} \gtrsim 1$). This behavior is governed by the magnitude of strain variation allowed per cycle: short cycles limit both diffusion and viscoelastic evolution, resulting in smaller strain amplitude and therefore fewer slip events, whereas longer cycles allow larger variations in elastic, viscoelastic, and hygroexpansive strains, thereby promoting slip accumulation. The same

reasoning applies to viscoelastic effects: even when diffusion is fast, shorter cycles limit the evolution of moisture-dependent compliance, reducing the mechanosorptive response (see data points for $Fo_{\chi}^{99} = 3.22$). In summary, the closer the system is to equilibrium within each cycle, the higher the mechanosorptive contribution to the total strain.

The fitted parameters further quantify the relative importance of the governing processes. Diffusion has a dominant influence, contributing approximately 7 × more than viscoelasticity ($a/b \approx 6$), as it controls not only hygroexpansion but also the evolution of elastic and viscoelastic compliances. The influence of ramping time is generally smaller but not negligible. While negligible in diffusion-dominated regimes ($Fo_{\chi}^{99} = 0.11$ or $Fo_{\chi}^{99} = 3.22$), T_r can lead to variations of up to 25% in intermediate regimes ($Fo_{\chi}^{99} \approx 1$–2), where many experimental campaigns lie.

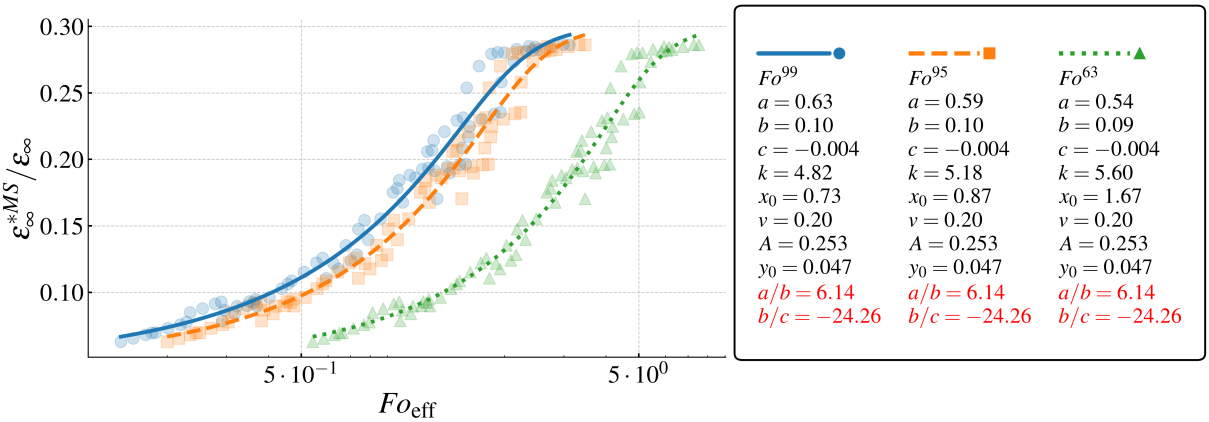

Fig. 8: Mechanosorptive contribution on total strain as a function of Fo_{eff} for characteristic relaxation times of $63, 95, 99$.

To analyze the choice of characteristic times T_{τ}^{Y} and T_{χ}^{Y} to the curve shown in Fig.7, the same procedure was repeated for different equilibration values, $Y = [63, 95]$. The result of this analysis is shown in Fig. 8. Small differences are evident when comparing the calculated Fo_{eff} values and the resulting curves. Despite differences in the fitting parameters, the ratio of the 3 main parameters, a, b, and c, remained constant. This result shows that the analysis is independent of the chosen characteristic-time used to define the dimensionless numbers.

To complement the analysis of the cumulated mechanosorptive strain, all systems were simulated for different loading degrees $\sigma/\sigma_c = [0.2, 0.7]$. The result is shown in Fig. 9 for $\varepsilon_{\infty}^{*MS}$ (colored markers) and its decomposed recoverable part, $\varepsilon_{\infty}^{*MSr}$ (green region), and non-recoverable part, $\varepsilon_{\infty}^{*MSnr}$ (red region). It is evident that exponential behavior is expected as the load level increases, until the first systems fail at $\sigma/\sigma_c \approx 0.8$. It is also evident that even at low loading levels ($\sigma/\sigma_c = 0.2$) a measurable mechanosorptive strain was observed. This highlights that even for small loads, the cumulated effect of constant load combined with moisture changes differs from the sum of their individual effects. As linearity is usually considered for viscoelastic and mechanosorptive tests within $\sigma/\sigma_c = [0.3, 0.5]$, a linear regression was performed for every system within this interval. As a result, an average $\langle R_{0.3-0.5}^2 \rangle = 0.99$ was found, showing that a linear relationship between ε^{MS} and σ/σ_c is acceptable in this interval. Finally, it is evident that the model develops predominantly recoverable mechanosorptive strains at low load levels, while the

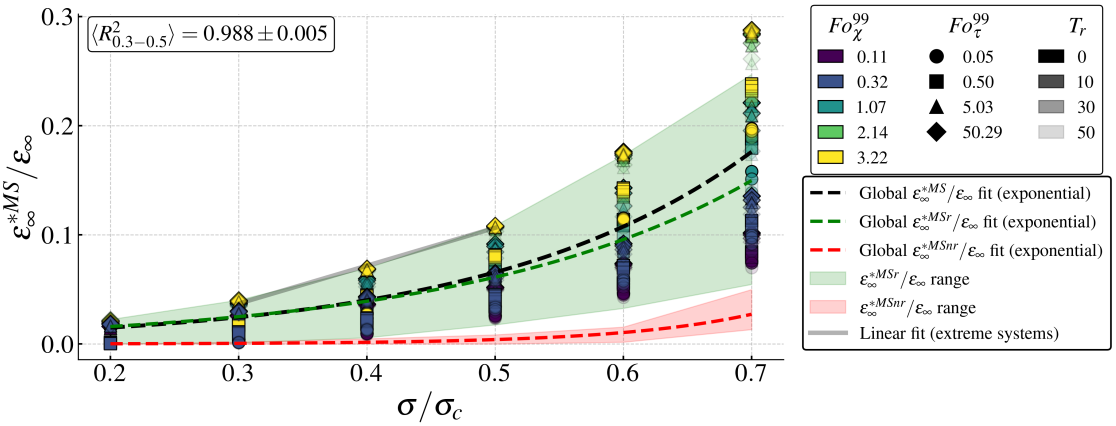

Fig. 9: Mechanosorptive strain dependence on loading degree σ/σ_c. The gray lines represent linear regressions performed within $\sigma/\sigma_c = 0.3$ and $\sigma/\sigma_c = 0.5$, and the average coefficient of determination obtained from the fits, $\langle R^2_{0.3-0.5} \rangle$, is shown.

non-recoverable component gradually increases with increasing load. As the system approaches failure, an abrupt rise in non-recoverable strain is accompanied by a reduction in the recoverable contribution (upper bounds of the green and red regions for $\sigma/\sigma_c \geq 0.65$). This decomposition indicates that the system initially accommodates recoverable mechanosorptive deformations, reaching a saturation point beyond which additional deformation is primarily non-recoverable, ultimately leading to failure.

3.3 Moisture Gradient Effects in Mechanosorption

To assess the role of moisture gradients in mechanosorption, all simulations from Sec. 3.2 were repeated using uniform moisture fields, where the bundle average moisture evolution was applied to all the fibers in the bundle. This preserves the macroscopic mean moisture history as in Sec. 3.2, while eliminating internal gradients. In this section, the properties of uniform-moisture systems are denoted with an overbar (e.g., $\bar{\varepsilon}$ for total strain), whereas non-uniform systems retain their original notation (e.g., ε).

Heterogeneities in the moisture field lead to fibers with different hygroexpansive strains and, under a global load-sharing scheme, introduce hygric stresses. This hygric stresses result in varying elastic strains, which influence the distribution of slip events within the bundle, even though hygroexpansive strains are not explicitly included in the slip condition (Eq. 4). This effect is shown in Fig. 10a, where the slip-strain per fiber is displayed immediately after a drying period and just before unloading. For the non-uniform moisture field (Fig. 10a left), a radial dependence of slip strains is observed, with higher local values compared to the uniform case (Fig. 10a right). This behavior is further highlighted in Fig. 10b, where averaging shows increased slip strain in the central region, but reduced values towards the periphery. Moreover, the non-uniform system exhibits a higher number of broken fibers, whose slip strains have been released. The combination of these effects resulted in a lower mean slip strain in the system with non-uniform moisture profile when compared to the uniform system.

The lower slip strain in systems with moisture gradients is reflected in the stable mechanosorptive strain, $\varepsilon^{*MS}_{\infty}$, as shown in Fig. 10c. The ratio between uniform

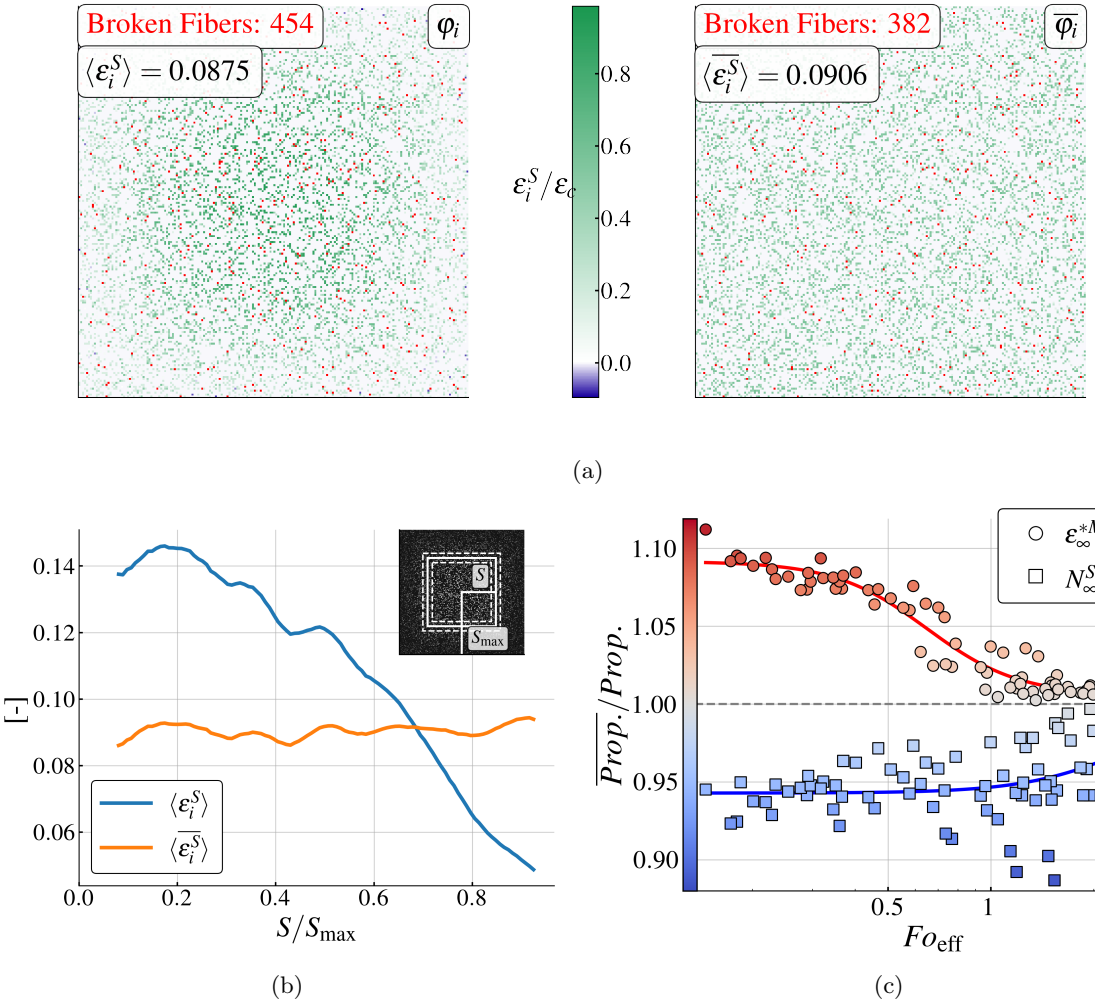

Fig. 10: a) Heat map of local slip strains for a non-uniform moisture field (left) and an uniform one (right), with broken fibers shown in red; b) average rolling window of slip strain for varying distance to the bundle center (see inset); c) Ratios of maximum mechanosorptive strain ($\bar{\varepsilon}_\infty^{MS}/\bar{\varepsilon}_\infty$) and total number of slips before unloading ($\bar{N}_\infty^S$) between simulations with and with uniform and non-uniform moisture fiels.

and non-uniform systems is plotted as a function of Fo_{eff} for both the relative mechanosorptive strain, $\varepsilon_\infty^{*MS}/\varepsilon_\infty$, and the number of slips, N_∞, both before unloading. Moisture gradients lead to a higher number of slip events in the bundle ($\bar{N}_\infty^S/N_\infty^S < 1$), while reducing the resulting $\varepsilon_\infty^{*MS}/\varepsilon_\infty$. This reflects a redistribution of slip activity: although gradients promote forward slip, they also enhance reverse slip, facilitated by the direction-dependent parameter Γ_β (Sec. 2.1). Despite this non-trivial effect, the overall differences remain small, with a maximum difference of approximately 10 %, primarily at low Fo_{eff} where mechanosorptive strains are already limited (Fig. 7). These results indicate that moisture gradients are not the primary factor governing mechanosorption.

3.4 Comparison to Experimental Data

Finally, to demonstrate the applicability of the model under realistic conditions, it is fitted to mechanosorptive data of Norway spruce samples in the radial direction, based on the parameters reported by Ferrara and Wittel (2025b). For the fitting procedure, the hygroexpansion coefficient α, the elastic dry and wet compliances

(C_d, C_w), and the viscoelastic dry compliance J_d are fixed based on literature values reported in Ferrara and Wittel (2024, 2025a). This choice is motivated by the expected level of stick-slip activity involved in their experimental determination. The elastic compliances are obtained from the initial linear regime of scleronomous tests and therefore exclude nonlinear stick-slip effects. The dry-state viscoelastic parameters are assumed to approximate intrinsic fiber behavior, since low stick-slip activity is expected for low moisture levels (see Sec. 3.1). The wet-state responses, nonetheless, require explicit consideration of bundle-level mechanisms. Accordingly, the wet compliance J_w and the stick-slip bundle parameters—namely the Weibull parameters λ and m, degradation parameters d and κ^f, and the moisture- and direction-dependent scaling factors Γ_m and Γ_β—are calibrated against the mechanosorptive and wet creep responses reported in the reference studies.

The calibration is based on two objective functions, defined from mechanosorptive and creep responses,

$$E_{MS} = \frac{1}{N}\sum_{i=1}^{N}\left(\varepsilon(t_i) - \varepsilon_{ref}(t_i)\right)^2, \tag{14}$$

$$E_{KV} = \left(J_{eff} - J_{ref}\right)^2, \tag{15}$$

$$E_{tot} = \tilde{E}_{MS} + \tilde{E}_{KV}, \tag{16}$$

where ε_{ref} is the reference total strain curve and J_{ref} is the reference wet compliance, and $\tilde{E}_{MS}$ and $\tilde{E}_{KV}$ denote the independently normalized errors.

Due to the large number of free parameters and the complexity of the model response, a staged surrogate-based optimization strategy was adopted. The procedure was structured in three steps: (i) a coarse search to identify non-viable regions and locate promising regions based on mechanosorptive response; (ii) a surrogate-guided refinement combining mechanosorptive and viscoelastic behavior to define an optimal parameter region; and (iii) a final sampling of this reduced region to determine the best-performing parameter set. *First*, a total of 500 parameter sets were generated using Latin hypercube (LHC) sampling within the bounds defined in Tab. 2. For each set, mechanosorptive simulations were performed under experimental conditions (9 moisture cycles, 2 MPa), and evaluated using E_{MS}, with additional penalties applied to failed simulations. *Second*, a surrogate model is trained on the generated data and proposes a 2000 candidate parameter sets to be evaluated using both mechanosorptive and creep responses. The creep behavior was assessed under 1 MPa ($\approx$ 25% of experimental σ_c) through the effective compliance J_{eff}, and scored using E_{KV}. This step enables the identification of parameter combinations that simultaneously reproduce both mechanosorptive and viscoelastic behavior. *Finally*, an optimal parameter region was defined from the 10 best-performing candidates based on the combined normalized error E_{tot}. The mean and standard deviation of these candidates were used to define a reduced parameter space, from which 100 additional systems were sampled using LHC. The final parameter set was selected as the candidate minimizing E_{tot} within this refined region.

Beyond calibration, the procedure provides insight into parameter influence. A Sobol analysis shows that J_w and λ dominate the model response, with total indices of 0.93 and 0.71, respectively, followed by m and Γ_m (0.13 and 0.08), while Γ_β, d,

Table 2: Parameter bounds used for the surrogate-based optimization, the resulting optimal interval, and the final selected parameter set.

Parameter	Tested interval	Optimal value	Final candidate
J_w	$[7.57 \times 10^{-4}, 1.0 \times 10^{-2}]$	$6.4(3) \times 10^{-3}$	5.9×10^{-3}
m	[1.1, 2.0]	1.28(14)	1.12
λ	$[5.0 \times 10^{-3}, 5.0 \times 10^{-1}]$	$5.3(3) \times 10^{-2}$	4.9×10^{-2}
d	[1.0, 80.0]	18(10)	29
κ^f	[0.05, 0.8]	0.6(1)	0.5
Γ_m	[0.40, 1.00]	0.50(3)	0.51
Γ_β	[0.40, 1.00]	0.74(9)	0.82

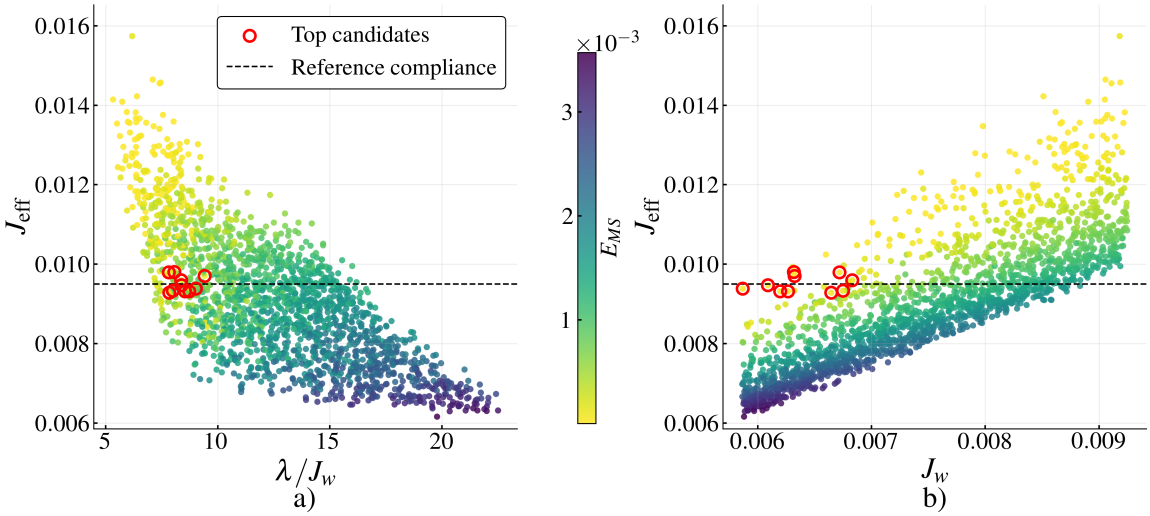

Fig. 11: Relations between the dominant input parameters J_w and λ and the model response. (a) Effective compliance J_{eff} as a function of the ratio λ/J_w, colored by the mechanosorptive error E_{MS}. (b) J_{eff} as a function of J_w, also colored by E_{MS}. Circled points indicate the selected 10 optimal candidates.

and κ^f have negligible influence (below 0.001). The interplay between J_w and λ is shown in Fig. 11. The ratio λ/J_w controls the balance between slip threshold magnitude and bundle compliance: low values promote stronger stick-slip activity. As shown in Fig. 11a, good agreement with mechanosorptive data is only obtained at low λ/J_w, indicating that significant slip activity is required to reproduce the mechanosorptive response. However, this increased slip activity also raises J_{eff}, leading to an overestimation of the reference compliance (Fig. 11b). This identifies a narrow region in parameter space (data points highlighted in red in Fig. 11) where the competing effects of viscoelastic compliance and stick-slip activity are balanced.

The mechanosorptive response with the optimal parameter set and the resulting strain decomposition are shown in Fig. 12, where the reference strain and its decomposition (based on the model used in Ferrara and Wittel (2025b)) are shown in black; the fiber-level DD-SS-FBM strains are shown in red; and the DD-SS-FBM strains, but with the decomposition protocol presented in Sec. 2.4 and representing bundle-level strains, are shown in blue. The total strain response in Fig. 12(a) shows good agreement between the model and the reference, capturing both loading and unloading cycles. The mechanosorptive contribution in Fig. 12(b) closely follows the evolution of the slip strain, indicating that the macroscopic response is

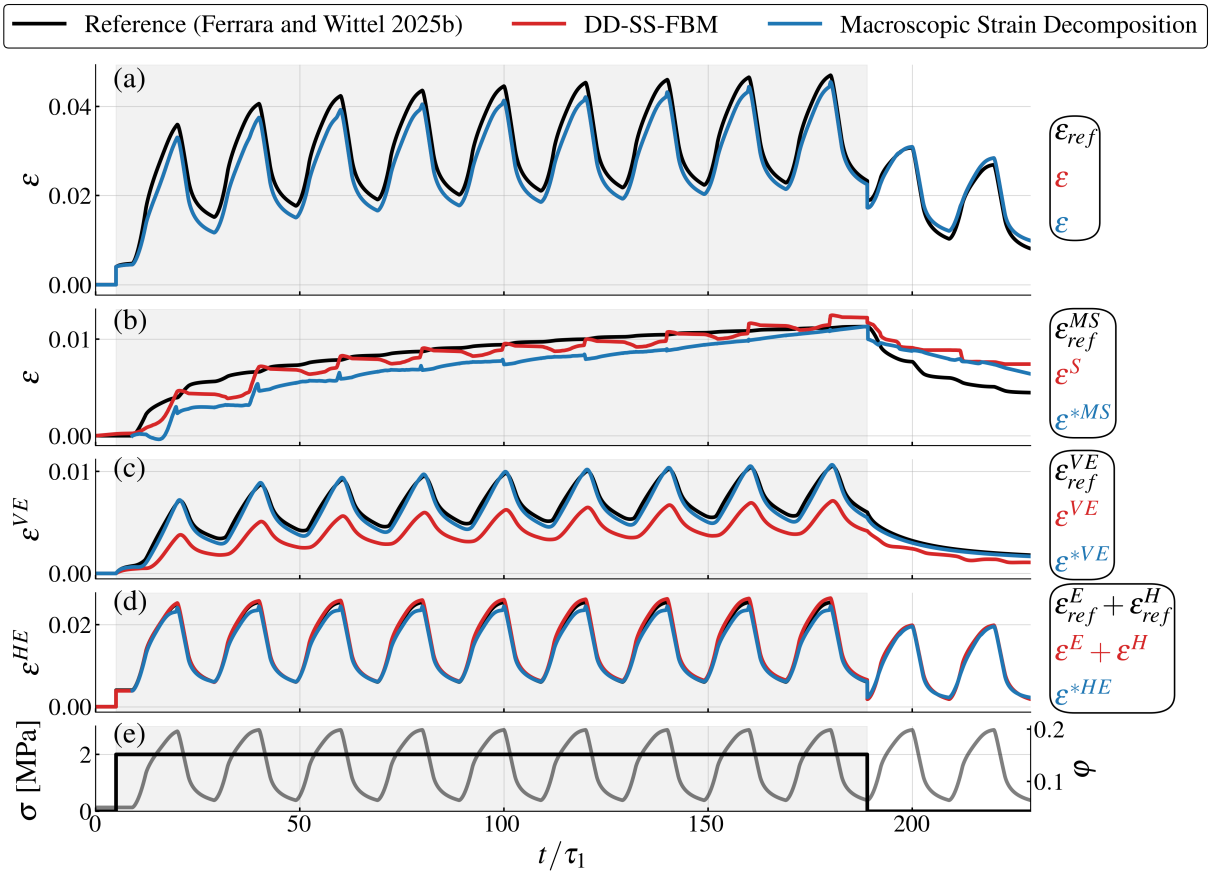

Fig. 12: Mechanosorptive response and strain decomposition of the optimal model, showing fiber-level (red) and bundle-level (blue) decompositions, compared to the reference strains (black) (Ferrara and Wittel 2025b).

primarily governed by cumulative stick-slip activity. The viscoelastic response at the bundle level (blue) closely follows the reference (black), reflecting the agreement between J_{eff} and J_{ref}, shown in Fig. 12(c). The evolution of the elastic and hygroexpansive contributions shows a minor but consistent increase over successive cycles, indicating progressive fiber failure and a corresponding increase in bundle compliance for the fiber-level properties (red curve in Fig. 12(d)). This highlights the role of irreversible material degradation in the overall response.

Beyond the overall agreement, deviations from the reference indicate the presence of additional mechanisms that the model can investigate. As an example, an initial negative mechanosorptive strain, ε^{*MS}, is observed during the first cycle (see Fig. 12(b)). A similar trend is reported experimentally by Ferrara and Wittel (2025b), but it cannot be captured by the moisture-dependent Kelvin-Voigt elements used to represent mechanosorption. Within the DD-SS-FBM, this behavior arises from transient viscoelastic effects under strong moisture gradients: during moistening, local compressive stresses induce a temporary back-deformation, that relaxes as the gradients vanish, and is most pronounced during the first cycle. This effect is further reflected in Fig. 12(c), where the fiber-level response (red) exhibits fluctuations during the unloading phase caused by the moisture gradients.

Comparing the model's behavior with mechanical parameters based on the longitudinal direction of wood (Fig. 6) and with radial direction parameters (Fig. 12) reveals a clear difference in the evolution of mechanosorption. In the longitudinal-like case, most slip strain accumulates during the first moisture cycle

and converges after approximately three cycles, whereas in the radial-like case, the mechanosorptive strain continues to evolve even after multiple cycles. This difference is attributed to the relative contributions of elastic and viscoelastic compliances. In the longitudinal-like response, deformation is dominated by elastic compliance, leading to slip events concentrated during initial loading. In contrast, the radial-like response is governed by viscoelastic deformation, with J_w approximately one order of magnitude larger than C_d and J_d, such that moisture cycling induces stronger internal mechanical perturbations and sustained slip evolution.

4 Conclusion

In this work, the Moisture-Dependent Stick–Slip Fiber Bundle Model (Amando et al. 2024) was modified to include moisture transport simulations and address key open questions in mechanosorption. The framework enables the analysis of cyclic moisture time scales, internal moisture gradients, and their interaction with material response. Dimensionless numbers were introduced to unify different experimental conditions, and a strain decomposition based on experimental procedures (Ferrara and Wittel 2025b) enabled direct comparison with measurable quantities.

The main conclusions are:

- *Role of cyclic moisture period and time-scale competition:* Mechanosorption is governed by the interplay between the cyclic moisture period (T_c) and intrinsic material time scales, rather than by moisture amplitude alone. Short cycles limit internal evolution and reduce strain accumulation, while longer cycles promote compliance changes, stick-slip activity, and enhanced mechanosorption.
- *Unification through dimensionless framework:* The combined effects of diffusion, viscoelasticity, and ramping moisture time collapse onto a master curve described by Fourier numbers of diffusion Fo_χ, viscoelasticity Fo_τ, and their combination Fo_{eff}. Diffusion dominates, contributing approximately $7\times$ more than viscoelasticity due to its direct impact on material compliance.
- *Influence of moisture gradients:* Moisture gradients redistribute local deformation and increase slip activity, but their net macroscopic effect remains limited due to compensation between tension and compression regions. Therefore, moisture gradients cannot be the primary responsible for mechanosorption.
- *Comparison to experimental results:* The model successfully reproduces both creep tests at constant moisture content and mechanosorptive response using a single, consistent parameter set. The fitting procedure reveals that this simultaneous agreement is only achieved when significant stick-slip activity is present in the system. This indicates that discrete slip events are not a secondary effect but a necessary mechanism for reconciling time-dependent deformation under both constant and varying moisture conditions.
- *Origin of variability in experimental behavior:* Variability across experiments arises from the balance between elastic, viscoelastic, and hygroexpansive contributions. Systems dominated by elasticity (e.g. wood in longitudinal direction) show limited mechanosorption, while strong viscoelastic and moisture-dependent systems (e.g. wood in radial direction) amplify mechanosorption.

Overall, this framework links moisture transport, time-scale competition, and stick–slip mechanics within a unified approach, providing a scalable basis for interpreting mechanosorption across materials and conditions, and highlighting the value of mechanistic modeling for testing and understanding the governing physical mechanisms. Future extensions may include the introduction of moisture-rate-dependent stick-slip behavior, as well as heterogeneous fiber classes to represent growth-ring structures (earlywood and latewood). These developments would enable a different assessment of how transient moisture dynamics and spatial heterogeneity influence the mechanosorptive response.

Acknowledgements. The authors acknowledge financial support from the Swiss National Science Foundation under SNF grant 200021-192186, "Creep behavior of wood on multiple scales," and thank Prof. Ingo Burgert for supporting the project development, and Dr. Gerhard Dill-Langer from the University of Stuttgart for discussions that motivated the further investigation of the DD-SS-FBM, which resulted in this work.

Declarations

- Code availability: The code for the simulations and analysis are avaiable in Amando et al. (2026)
- Funding: Swiss National Science Foundation under SNF grant 200021192186 "Creep behavior of wood on multiple scales".
- Conflicts of interest/Competing interests: None.
- Authors' contributions: Conception and methodology: FKW, JOAB; Formal analysis and investigation: JOAB; Writing: original draft preparation: JOAB; review and editing: FKW; Supervision: FKW.

References

Alava, M. J., Nukala, P. K. V. V., and Zapperi, S. (2006). Statistical models of fracture. Advances in Physics, 55(3-4), 349-476. https://doi.org/10.1080/00018730300741518

Amando de Barros J, Wittel FK (2024) Unifying model for the rheological behavior of hygroresponsive materials. Phys Rev E 109:044139. https://doi.org/10.1103/PhysRevE.109.044139

Amando de Barros JO, Schwiedrzik J, Wittel FK (2025) Resolving discrepancies in wood micromechanics: Strain-mapped compression of tracheid wall micropillars. Compos Part A Appl Sci Manuf 199:109209. https://doi.org/10.1016/j.compositesa.2025.109209

Amando de Barros JO, Wittel FK (2026) DD-SS-FBM-2026: Diffusion-Dependent stick-slip Fiber Bundle Model. GitHub repository. https://github.com/juliobarros-BR/DD-SS-FBM-2026- (accessed April 2026).

Armstrong LD, Christensen G (1961) Influence of moisture changes on deformation of wood under stress. Nature 191:869. https://doi.org/10.1038/191869A0

Armstrong LD, Grossman P (1972) The behaviour of particle board and hardboard beams during moisture cycling. Wood Sci Technol. 6:128-137 https://doi.org/10.1007/BF00350826

Armstrong LD, Kingston RST (1960) Effect of moisture changes on creep in wood. Nature 185:862. https://doi.org/10.1038/185862C0

Bažant ZP (1985) Constitutive equation of wood at variable humidity and temperature. Wood Sci Technol 19(2):159-177. https://doi.org/10.1007/BF00353077

Bethe E (1969) Festigkeitseigenschaften von Bauholz bei Lagerung im Wechselklima unter gleichzeitiger mechanischer Belastung. Eur J Wood Wood Prod. 27:291-303 https://doi.org/10.1007/BF02612703

Boyd JD (1982) An anatomical explanation for visco-elastic and mechano-sorptive creep in wood, and effects of loading rate on strength. In: P. Baas (ed) New Perspectives in Wood Anatomy, 1st edn. Springer, Dordrecht, pp 171-222 https://doi.org/10.1007/978-94-017-2418-0_8

Cordeiro A (2025) Advancements in packaging materials: trends, challenges, and future perspectives. J Packag Technol Res 9:1-20. https://doi.org/10.1007/s43615-025-00586-4

Daniels HE (1945) The statistical theory of the strength of bundles of threads. I. Proc R Soc Lond A Math Phys Sci 183(995):405–435. https://doi.org/10.1098/rspa.1945.0011

Deshwal GK, Panjagari NR, Alam T (2019) An overview of paper and paper based food packaging materials: health safety and environmental concerns. J Food Sci Nutr 58:1-12. https://doi.org/10.1007/s13197-019-03950-z

Dill-Langer, G., Hidalgo, R. C., Kun, F., Moreno, Y., Aicher, S., and Herrmann, H. J. (2003). Size dependency of tension strength in natural fiber composites. Physica A: Statistical Mechanics and its Applications, 325(3-4), 547-560. https://doi.org/10.1016/S0378-4371(03)00141-9

Dong F, Olsson A-M, Salmén L (2010) Fibre morphological effects on mechano-sorptive creep. Wood Sci Technol 44:475-483. https://doi.org/10.1007/s00226-009-0300-3

Dubois F, Husson J-M, Sauvat N, Manfoumbi N (2012) Modeling of the viscoelastic mechano-sorptive behavior in wood. Mech Time-Depend Mater 16(4):439-460. https://doi.org/10.1007/s11043-012-9171-3

Eriksson L, Norén B (1965) Der Einfluß von Feuchtigkeitsänderungen auf die Verformung von Holz bei Zug in Faserrichtung. Holz als Roh-und Werkstoff 23(5):201-209 https://doi.org/10.1007/BF02612968

Ferrara A, Wittel FK (2024) Micro-mechanical tests on tissue slices of Norway spruce: tensile and shear performance. Holzforschung 78(11–12):624–630. https://doi.org/10.1007/s11043-025-09772-1

Ferrara A, Wittel FK (2025) Tensile creep of Norway spruce on the tissue scale. Mech Time-Depend Mater 29(2):36. https://doi.org/10.1007/s11043-025-09772-1

Ferrara A, Wittel FK (2026) Mechanosorptive creep of Norway spruce on the tissue scale perpendicular to grain. Holzforschung 80(4): 277-289. https://doi.org/10.1515/hf-2025-0115

Frandsen HL, Damkilde L, Svensson S (2007) A revised multi-Fickian moisture transport model to describe non-Fickian effects in wood. Holzforschung 61:563–572. https://doi.org/10.1515/HF.2007.085

Gibson E (1965) Creep of wood: role of water and effect of a changing moisture content. Nature 206:213. https://doi.org/10.1038/206213A0

Grottesi G, Coelho GBA, Kraniotis D (2023) Heat and moisture induced stress and strain in wooden artefacts and elements in heritage buildings: A review. Appl Sci 13(12):7251. https://doi.org/10.3390/app13127251

Gunderson DE, Tobey WE (1990) Tensile creep of paperboard—effect of humidity change rates. MRS Proc 197:213-226. https://doi.org/10.1557/PROC-197-213

Habeger CC, Coffin DW, Hojjatie B (2001) Influence of humidity cycling parameters on the moisture-accelerated creep of polymeric fibers. J Polym Sci B Polym Phys 39(17):2048-2062. https://doi.org/10.1002/polb.1180

Halász Z, Kun F (2009) Fiber bundle model with stick-slip dynamics. Phys Rev E 80(2):027102. https://doi.org/10.1103/PhysRevE.80.027102

Haslach HW (1994) The mechanics of moisture accelerated tensile creep in paper. Tappi J. 77(10):179-186.

Hearmon RFS, Paton JM (1964) Moisture content changes and creep of wood. For Prod J 14(8):357-359. https://doi.org/10.1007/PL00011084

Herrmann HJ, Roux S, editors (1990) Statistical Models for the Fracture of Disordered Media. North-Holland, Amsterdam.

Hidalgo RC, Kun F, Herrmann HJ (2002) Creep rupture of viscoelastic fiber bundles. Phys Rev E 65:032502. https://doi.org/10.1103/PhysRevE.65.032502

Hunt DG, Shelton CF (1987) Progress in the analysis of creep in wood during concurrent moisture changes. J Mater Sci. 22:313-320 https://doi.org/10.1007/BF01160586

Kun F, Zapperi S, Herrmann HJ (2000) Damage in fiber bundle models. Eur Phys J B Condens Matter Complex Syst 17:269–279. https://doi.org/10.1007/PL00011084

Maas JM, Wittel FK (2026) From Elasticity to Creep: Orthotropic moisture-dependent rheology of Norway spruce. Holzforschung 80(7):514-542. https://doi.org/10.31224/6321

Mårtensson A (1994) Mechano-sorptive effects in wooden material. Wood Sci Technol 28(6):437-449. https://doi.org/10.1007/BF00225463

Mårtensson A (1988) Tensile behaviour of hardboard under combined mechanical and moisture loading. Wood Sci Technol 22:129–142.

Moliński W, Raczkowski JW (1988) Mechanical stresses generated by water adsorption in wood and their determination by tension creep measurements. Wood Sci Technol. https://doi.org/10.1007/BF00386013

Niemz P, Teischinger A, Sandberg D (eds) (2023) Springer Handbook of Wood Science and Technology. Springer, Cham. https://doi.org/10.1007/978-3-030-81315-4

Olsson A-M, Salmén L, Eder M, Burgert I (2007) Mechano-sorptive creep in wood fibres. Wood Sci Technol 41(1):59-67. https://doi.org/10.1007/s00226-006-0086-5

Phoenix SL, Beyerlein IJ (2000) Statistical strength theory for fibrous composite materials. In: Kelly A, Zweben C (eds) Comprehensive Composite Materials, Vol 1. Elsevier, Oxford, pp 559-639. https://doi.org/10.1016/B0-08-042993-9/00056-5

Raczkowski JW (1969) Der Einfluß von Feuchtigkeitsänderungen auf das Kriechverhalten des Holzes. Eur J Wood Wood Prod. https://doi.org/10.1007/BF02612919

Ruzicka MC (2008) On dimensionless numbers. Chem Eng Res Des 86(8):835-868. https://doi.org/10.1016/j.cherd.2008.03.007

Salmén L, Fellers C (1996) Moisture-induced transients and creep of paper and Nylon 6,6: a comparison. Nord Pulp Pap Res J 11(3):186-191. https://doi.org/10.3183/npprj-1996-11-03-p186-191

Salmén L (2004) Micromechanical understanding of the cell-wall structure. C R Biol 327(9-10):873-880. https://doi.org/10.1016/j.crvi.2004.03.010

Salmén L, Burgert I (2009) Cell wall features with regard to mechanical performance. A review COST Action E35 2004-2008: Wood machining – micromechanics and fracture. Holzforschung 63(2):121-129. https://doi.org/10.1515/HF.2009.011

Salmén L (2015) Wood morphology and properties from molecular perspectives. Ann For Sci 72(6):679-684. https://doi.org/10.1007/s13595-014-0403-3

Salmén L (2022) On the organization of hemicelluloses in the wood cell wall. Cellulose 29:1-7. https://doi.org/10.1007/s10570-022-04425-9

Skaar C (1988) Wood-Water Relations. Springer, Berlin Heidelberg. https://doi.org/10.1007/978-3-642-73683-4

Sonderegger W, Vecellio M, Zwicker P, Niemz P (2011) Combined bound water and water vapour diffusion of Norway spruce and European beech in and between the principal anatomical directions. Holzforschung 65:819–828. https://doi.org/10.1515/HF.2011.091

Stevanic JS, Salmén L (2020) Molecular origin of mechano-sorptive creep in cellulosic fibres. Carbohydr Polym 230:115615. https://doi.org/10.1016/j.carbpol.2019.115615

Wang J, Cao X, Liu H (2020) A review of the long-term effects of humidity on the mechanical properties of wood and wood-based products. Eur J Wood Wood Prod 78:1-18. https://doi.org/10.1007/s00107-020-01590-0

Weibull W (1951) A statistical distribution function of wide applicability. J Appl Mech. 18(3):293-297 https://doi.org/10.1115/1.4010337

Zhang S, Ding E (1996) Failure of fiber bundles with local load sharing. Phys Rev B 53(2):646. https://doi.org/10.1103/PhysRevB.53.646

Zhang C, Keten S, Derome D, Carmeliet J (2021) Hydrogen bonds dominated frictional stick-slip of cellulose nanocrystals. Carbohydr Polym 258:117682.https://doi.org/10.1016/j.carbpol.2021.117682

A Numerical Implementation Details

This appendix summarizes the numerical procedures used to implement the coupled moisture-transport and DD-SS-FBM framework. The adopted strategies were designed to ensure numerical stability, accurately resolve the nonlinear stick-slip dynamics, and maintain computational efficiency across the large simulation campaigns performed in this work.

A.1 Moisture Transport Implementation

The diffusion process was solved only on a triangular domain corresponding to one-eighth of the fiber bundle cross-section, representing the minimal symmetry group of the square lattice. This reduced domain was used to decrease computational cost and memory usage. The resulting moisture fields were subsequently mirrored and mapped onto the full bundle geometry for the coupled mechanical simulations.

The moisture field was updated incrementally using the explicit discretization of Eq. 5,

$$\varphi_i^{t+\Delta t} = \varphi_i^t + \frac{\chi_i^t \Delta t}{\Delta l^2} \sum_{j \in \mathcal{N}_i} \left(\varphi_j^t - \varphi_i^t\right), \tag{17}$$

where $\mathcal{N}_i$ denotes the set of nearest neighbors of fiber i, and Δl is the spatial discretization distance between adjacent fibers. The bundle geometry was normalized such that $\Delta l = 1$.

Numerical stability of the explicit scheme was ensured through the Courant–Friedrichs–Lewy condition,

$$\Delta t \leq \frac{0.25}{\Delta l^2 \max(\chi_i)}. \tag{18}$$

At each diffusion step, the fiber with the highest local diffusivity, $\max(\chi_i)$, was used to determine the admissible time increment. Within this stability bound, the diffusion time step was adaptively updated throughout the simulation to maximize computational efficiency.

A.2 Mechanical Solver and Coupled Time Integration

To accurately resolve the nonlinear stick–slip response of the DD-SS-FBM, the bundle's initial mechanical loading was precomputed using an event-driven algorithm: the most critical fiber was identified, the minimum load increment required to trigger slip was applied, the slipped fiber was updated, and the redistributed load field was recalculated until no further slips occurred, this lowest-threshold loading procedure was repeated until bundle failure. This procedure was repeated for the bundle on dry and wet states, the resulting slip and load evolution on dry state were stored and used as initialization data for subsequent simulations at prescribed load levels. The critical load and strain on the wet state were used to normalize all reported stresses and strains.

The coupled hygro-mechanical evolution was then solved incrementally in time. Moisture histories were resampled into 100 increments per moistening/drying segment. At each increment, the updated moisture field was applied, viscoelastic strains were updated, forces were redistributed, and the slip criterion was evaluated.

To properly resolve slip avalanches occurring within a time increment, an adaptive recursive substepping scheme was employed. Whenever multiple slip events were triggered within a single step, the step was bisected and the solution repeated using moisture fields obtained by linearly interpolating the local moisture of each fiber. Recursive bisection was allowed up to 10 times; beyond this limit, the step was accepted to avoid excessive computational cost. Depending on the severity of avalanche activity, a single moisture cycle could therefore require up to 10^5 effective time steps.

B Symbol List

Table 3: Summary of notation used in the DD-SS-FBM. Symbols are grouped by physical meaning.

Mechanical and Rheological Quantities	
$D(\varphi_i)$, $J_n(\varphi_i)$, $J(\varphi)$, τ_n, α	Elastic compliance, viscoelastic compliances (KV elements), sum of individual viscoelastic compliances (sum of KV elements), viscoelastic relaxation times and hygroexpansion coefficient
σ_i, F_i, σ_c	Fiber stress, force, and critical stress
ε_i, ε, ε_∞	Fiber strain, total bundle strain, and stabilized strain
ε_i^E, ε_i^{VE}, ε_i^H, ε_i^S	Elastic, viscoelastic, hygroexpansive, and slip strain components (fiber level)
ε^E, ε^{VE}, ε^H, ε^S, J_{eff}	Elastic, viscoelastic, hygroexpansive, and slip strain components (bundle average), and bundle effective viscoelastic compliance
ε_c, σ_c	Critical strain and stress, based on the model at wet state
Statistical and Model Parameters	
$\varepsilon_i^{th}(j)$, k_i, β_i	Slip threshold, number of slips, and slip direction
N, A_i	Number of fibers and fiber area (normalized to 1)
m, λ	Weibull shape and scale parameters
d, κ^f	Slip degradation parameter and failure limit
Γ_φ, Γ_β, $f(k)$	Moisture/direction scaling factors and history weakening function
Moisture Transport	
φ_i, φ_0, $\langle\varphi\rangle$	Local, initial, and average moisture content
φ_d, φ_w, $\varphi_{\text{env}}(t)$	Dry/wet moisture states and environmental boundary condition
$\chi_i(\varphi_i)$	Moisture-dependent diffusion coefficient
Ω_{cen}, Ω_{out}	Central and boundary fiber subsets
Time Scales and Dimensionless Numbers	
T_c, T_r	Moisture cycle period and ramping time
T_χ^Y, T_τ^Y	Characteristic diffusion and viscoelastic times (criterion Y)
Fo_χ^Y, Fo_τ^Y, Fo_{eff}^Y	Diffusion, viscoelastic, and effective Fourier numbers
a, b, c, Y	Weighting parameters and equilibration threshold
Macroscopic Decomposition (Experimental)	
ε^{*VE}, ε^{*HE}, ε^{*MS}, ε^{*R}, ε^{*P}	Viscoelastic, hygroelastic, mechanosorptive, reduced and plastic strains (post-processed)
ε^{*MSr}, ε^{*MSnr}, ε_∞^{*MS}	Recoverable, non-recoverable, and stabilized mechanosorptive strain
N_∞^S, C_L, C_U	Total number of slips at stabilization; number of loaded/unloaded cycles
Fitting Quantities	
$\varepsilon_{\text{ref}}(t)$, J_{ref}	Reference strain curve and compliance from Ferrara and Wittel (2025b)
E_{MS}, E_{KV}, E_{tot}	Error measures for mechanosorptive, viscoelastic, and total fit

C Simulation Seed Comparison

To ensure representation of the analyzed results in this work, the simulations analyzed in Sec. 3.2 were repeated for 3 different seeds to generate the Weibull slip threshold distribution. The result of Fig 7 is repeated with all seeds, and the result in 13 shows that the result is consistent throughout all tested seeds.

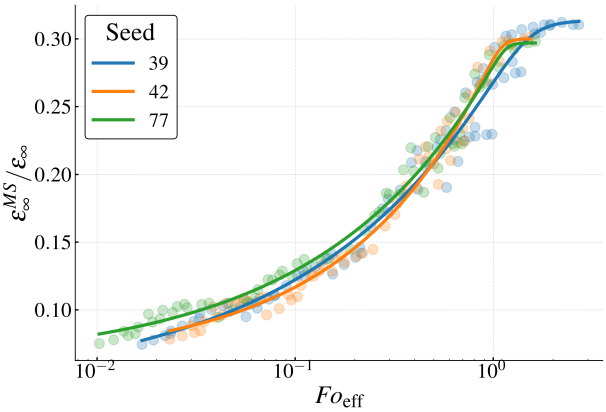

Fig. 13: Comparison of Fo_{eff} calculation for different seeds to generate the slip threshold distribution. The blue curve is the seed used through the manuscript (39), while the others were used for this comparison.